PAPER

Check for updates

Crystallographic facet engineering of ZnO nanoparticles for photocatalytic organic pollutant degradation and antibacterial activity†

Priya Paul,[ab] Fataha Nur Robel,[b] Newaz Mohammed Bahadur,[c] Sumaya Tabassum, [a] Subarna Sandhani Dey,[d] Muhammad Shahriar Bashar,[e] Nazmul Islam Tanvir,[f] Samina Ahmed [*a] and Md. Sahadat Hossain [*a]

Utilizing crystallographic engineering, dual-functional zinc oxide nanoparticles (ZnO-NPs) are revealed to have superior antimicrobial and photocatalytic properties. They surpass traditional ZnO (20–40% degradation, <25 mm zones) by achieving 34 mm inhibition zones against *Staphylococcus aureus* and 50% Congo red degradation under visible light. Four distinct synthesis methods were used to create the facet-tuned NPs: PEG-assisted co-precipitation (Z1), oleic acid-modified hydrothermal (Z2), conventional hydrothermal (Z3), and *Canna indica*-mediated green synthesis (Z4). XRD analysis revealed that Z1/Z3 (crystallite size: 34.40–36.69 nm, microstrain: 0.1334–0.1394) and Z2/Z4 (84.51–97.20 nm, microstrain: 0.0611–0.0816) grew preferentially in the (101)/(103) and (112)/(110) planes, respectively. FESEM showed that the performance of nanodiscs (Z1), cubic rods (Z2), plate-needle hybrids (Z3), and nanorods (Z4) depended on their morphology. While FTIR found residual C=O/C−O groups impacting surface contacts, EDX verified high Zn purity (>86%). Defect-rich E2 (high) phonon modes (439 cm^{-1}) were validated by Raman spectroscopy, confirming defect-mediated charge separation, which is essential for photocatalytic effectiveness. The effectiveness of Z2/Z4 was demonstrated by antibacterial tests (34–26 mm against *S. aureus* and 18–10 mm against *E. coli*), using nanorod-driven membrane penetration and Zn^{2+} release. The dual function of the (112) plane, which connects the production of ROS and the inhibition of bacteria, creates a model for ZnO-NPs of the future in the fight against healthcare infections and water pollution.

Introduction

Nanoparticles have emerged as pivotal materials in modern science and technology due to their unique physicochemical properties, which arise from their high surface-area-to-volume ratio and quantum confinement effects.[1] Among these, zinc oxide nanoparticles (ZnO-NPs) have attracted a lot of interest

a Institute of Glass & Ceramic Research and Testing, Bangladesh Council of Scientific and Industrial Research (BCSIR), Dhaka 1205, Bangladesh. E-mail: shanta_samina@yahoo.com, saz8455@gmail.com

b Department of Applied Chemistry and Chemical Engineering, Noakhali Science and Technology University, Noakhali, Bangladesh

c Department of Chemistry, Noakhali Science and Technology University, Noakhali, Bangladesh

d Institute of Food Science and Technology (IFST), Bangladesh Council of Scientific and Industrial Research (BCSIR), Dhaka, Bangladesh

e Institute of Energy Research & Development, Bangladesh Council of Scientific and Industrial Research (BCSIR), Dhaka 1205, Bangladesh

f Industrial Physics Division, Bangladesh Council of Scientific and Industrial Research (BCSIR), Dhaka 1205, Bangladesh

† Electronic supplementary information (ESI) available. See DOI: https://doi.org/10.1039/d5ma00316d

due to their numerous uses in optoelectronics, photocatalysis, antimicrobial agents, and sensors.[2] With its massive exciton binding energy (60 meV) and wide bandgap (~3.37 eV), ZnO is a semiconductor that possesses remarkable optical, electrical, and catalytic capabilities.[3] The structural features of ZnO-NPs, such as crystallite size, morphology, dislocation density, and—most importantly—the orientation of the crystallographic planes, have a significant impact on their functional effectiveness.[4] Through structural alterations and synthesis techniques, these factors can be precisely tailored to govern their performance in specific applications, like microbial suppression and dye degradation.[5–7]

The significance of crystallographic engineering in maximizing material functionality is highlighted by recent developments in nanotechnology.[8] The hexagonal wurtzite structure is used to index the crystallographic planes in ZnO; the most notable of these are the (100), (002), (101), (102), (110), and (103) planes. Surface reactivity, charge carrier dynamics, and modes of interaction with biological or environmental systems are determined by the exposure of particular crystal planes in ZnO-NPs.[9] For example, the (101) plane's high atomic density and defect-rich surfaces, which promote electron–hole pair

separation, are linked to increased photocatalytic activity.[10,11] Because of its high atomic density and favoured *c*-axis orientation, the (002) plane improves photocatalytic degradation efficiency by increasing electron mobility and decreasing charge recombination.[12] On the other hand, the (110) and (103) planes have been linked to increased surface reactivity, which qualifies them for use in photocatalysis and antimicrobial applications.[13]

Synthesis techniques and structural alterations have a significant impact on the development and dominance of particular ZnO crystal planes. Different morphological and crystallographic traits are introduced by each approach. For instance, certain crystal facets can be stabilized by surfactant-assisted synthesis (such as polyethylene glycol, or PEG), and crystallite development and strain are influenced by calcination temperature.[14] Furthermore, surface chemistry is altered by the application of capping agents such as oleic acid or natural extracts, which further fine-tune interfacial interactions.[15,16] While surfactant-assisted synthesis can preferentially improve the (100) or (103) planes by altering surface energy dynamics, hydrothermal synthesis frequently produces the preferential creation of the (002) and (101) planes due to regulated nucleation and growth kinetics.[17,18] Green synthesis techniques, which make use of bio-templates or plant extracts, have been shown to affect crystal facet exposure *via* biomolecular interactions, which further affect functional characteristics.[19] These changes affect dislocation density, microstrain, and preferred growth orientations, which together define functional results, in addition to controlling nanoparticle size and form.

This study's recent results present a novel relationship between ZnO's dual use in photocatalysis and antibacterial activity and its crystal plane expansion. Together with the (101), (103), and (110) planes, the emergence of the (112) plane is a crucial element impacting both functionalities. Stronger interactions with bacterial membranes are made possible by the high surface energy and defect density of this recently discovered plane, which are linked to the (112) plane and increase antibacterial efficacy. Gaining insight into and managing the creation of this crystal facet creates new opportunities for ZnO-based nanomaterial optimization, providing improved performance in biomedical and environmental applications. The logical design of ZnO nanoparticles with exceptional multifunctional capabilities is made possible by the insightful information this study offers on crystal facet engineering.

2. Materials and methods

2.1 Materials

The precursor chemicals were $Zn(NO_3)_2 \cdot 6H_2O$ (zinc nitrate hexahydrate), 98%, purchased from "Fluka", and "Commercial grade" NaOH (sodium hydroxide) was used. Polyethylene glycol 400 (average molecular weight ~400, liquid) was purchased from Labtex, and Ultrapure Oleic acid from "Sigma-Aldrich". *Canna indica* leaves were collected from the garden of BCSIR, Dhaka, Bangladesh. Ethanol was bought from E-Merck Germany. Deionized water (prepared by double distillation) was used in all the experiments.

2.2 Experimental details

To get ZnO-Np modified with PEG in a mortar and pestle, 2.26 g of $Zn(NO_3)_2 \cdot 6H_2O$ and 0.75 g of NaOH were ground together. After 5 minutes, 1.5 mL of PEG was added, and the mixture was processed once again for 30 minutes. Following an hour of sonication, the sample was rinsed twice with DI and once with ethanol. After being collected, the sample (Z1) was dried at 70 °C and cooked in a furnace for two hours at 320 °C.

Oleic acid-modified ZnO was prepared by combining 0.5 M $Zn(NO_3)_2 \cdot 6H_2O$ with 1 M NaOH and stirring for approximately half an hour using a magnetic stirrer. A total of 40 mL of mixture was sonicated for 45 minutes after 1 mL of oleic acid was added while stirring. The mixture was sonicated and then placed in an autoclave, where it was heated to 180 °C for three hours. The precipitation was separated by centrifuging the solution for 15 minutes at 7000 rpm, and it was then freeze-dried for the entire night. Finally, Z2 was calcined for 4 hours at 500 °C after drying.

In order to perform the hydrothermal synthesis procedure, 0.2 M $Zn(NO_3)_2 \cdot 6H_2O$ was combined with 4 M NaOH to make up an 80 mL solution and autoclaved for three hours at 180 °C. Decanting the surplus water separated the resultant precipitate, which was then oven-dried at 105 °C. Phase developments were examined by calcining the resulting powders at 500 °C. Zinc oxide (Z3) from hydrothermal synthesis is thus produced.

Finally, the leaves of the *Canna indica* plant were dried and pulverized into a powder. To obtain the extract, 1.8 g of powdered leaf was gathered in 36 mL of water and heated to 80 °C for one hour. Following this, the extract was separated and combined with $Zn(NO_3)_2 \cdot 6H_2O$ in a ratio of 4.5 : 1 until a thick paste was formed. The paste was then put in a crucible and calcined for four hours at 500 °C. Z4 is the name of the obtained sample.

2.3 Characterization

2.3.1 X-Ray diffraction analysis. Crystallographic characterization of the synthesized nanoparticles was performed using the Rigaku SE equipment, which has a scan range of 5° to 70° and a step width of 0.01. The radiation source was a ceramic copper tube with a wavelength of 1.5406 Å, an accelerating voltage of 40 kV, and a current of 50 mA. The operating temperature of the cooling water was between 19 and 20 °C. A silicon reference standard was used to assess the accuracy of the instrument. Using card number 00-005-0664, the ZnO nanoparticle data and the data from the ICDD database were compared.

2.3.2 Analysis of surface morphology using FESEM. Using field emission with high resolution utilizing a JEOL JSM-7610F scanning electron microscope with EDX capabilities, the surface properties of the produced ZnO nanoparticles were examined. All of the samples were covered with gold to continue examining their surface characteristics, and images were taken at a potential of 15 kV build-up. Following the gold covering, the obtained samples were put in a dual-sided carbon-capped container and submerged in an ethanol solution.

2.3.3 FTIR spectrometric analysis. Functional groups found in ZnO-NPs were distinguished from one another in the FTIR

spectra using an FTIR spectrophotometer (IR-Prestige 21, Shimadzu, Japan) equipped with an attenuated total reflection (ATR) attachment. The results' transmittance mode, with a spectral resolution of 4 cm^{-1}, was maintained between 400 cm^{-1} and 4000 cm^{-1}. The data that is shown includes an average of thirty scans.

2.3.4. Raman analysis. To validate the purity and phase density of the samples, Raman analysis was done with a laser power adjustable from 7 to 450 mW. The measurements were carried out on a HORIBA MacroRAM Raman spectrometer at an excitation wavelength of 785 nm, guaranteeing accurate identification of the ZnO vibrational modes.

3. Results & discussion

3.1 Crystallographic analysis

The crystallographic phases of samples Z1, Z2, Z3, and Z4 were confirmed by comparing their diffraction patterns with the standard ICDD card no. 00-005-0664. Throughout the samples, the distinct peaks, matching Miller indices, and peak locations were all quite consistent (Fig. 1). The sizes of the crystallites determined by various techniques differed greatly. The crystallite sizes varied from 34.40 nm to 97.20 nm, according to the Scherrer equation. The size range of the Williamson–Hall (W–H) plot was 35.56 nm to 66.02 nm, and the strain values (derived from the uniform deformation model) ranged from −0.0006 to 0.0012. The energy density ranged from 4.81 J m^{-3} to 51.01 J m^{-3}, while
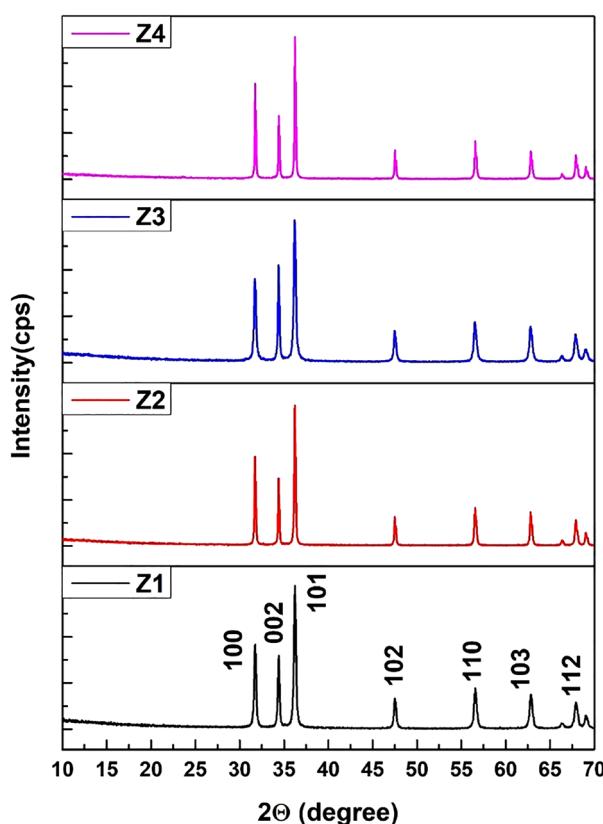
the stress values, which were determined using the uniform stress deformation model, ranged from −0.1691 GPa to 0.0520 GPa. The Halder–Wagner approach estimated crystallite sizes between 25.64 nm and 34.48 nm, while the size-strain plot (SSP) method produced sizes between 35.55 nm and 47.81 nm. Values from the Monshi–Scherrer method ranged from 35.37 nm to 52.76 nm. The Sahadat–Scherrer and LSLMSE approaches, on the other hand, produced sizes larger than 100 nm, which were not appropriate for these materials. Eqn (1)–(6) is applied to calculate the crystallite sizes.[20]

$$\text{Scherrer equation, } D = \frac{K\lambda}{\beta \cos \theta} \tag{1}$$

$$\text{Williamson–Hall equation, } \beta_{\text{total}} \cos \theta = K\beta\lambda D_{\text{W}} + 4\varepsilon \sin \theta \tag{2}$$

$$\text{Stress, } \sigma = Y_{hkl}\varepsilon \tag{3}$$

$$\text{Energy density, } \mu = \varepsilon^2 \frac{Y_{hkl}}{2} \tag{4}$$

$$\text{Sizestrain equation, } (d_{hkl}\beta_{hkl}\cos\theta)^2 = \frac{K_{\text{B}}\lambda}{D_{\text{w}}}(d_{hkl}^2\beta_{hkl}\cos\theta) + \frac{\varepsilon^2}{4} \tag{5}$$

$$\text{Halder–Wagner equation, } \left(\frac{\beta_{hkl}\cos\theta}{2\sin\theta}\right)^2 = \frac{1}{D_{\text{w}}}\frac{\beta_{hkl}\cos\theta}{(2\sin\theta)^2} + (2\varepsilon)^2 \tag{6}$$

In this context, D is the crystallite size, and β is the full width at half maximum measured in radians. The crystallite shape factor is denoted as K, and although both instrumental and non-instrumental factors influence it, the widely accepted numerical value remains 0.90. λ is denoted for the X-ray Cu source wavelength, which is 1.5460 Å, and θ is denoted for the Bragg's angle of the diffraction peak. D_{W} denotes the crystallite particle's dimensions. Stress (σ) and strain (ε) are linked through Young's modulus Y_{hkl}. The modulus of elasticity for ZnO was found to be 140 GPa.

Preferred growth orientations and texture coefficients (TC) were computed for each of the four samples by using eqn 7 and 8. Sample Z1's highest TC values were found in the (1 0 1), (1 1 0), and (1 0 3) planes, with the (1 1 2) plane coming in second. With sample Z2, the (1 0 1), (1 1 0), (1 0 3), and (1 1 2) planes showed the desired growth, whereas the (1 1 2) planes had the greatest TC value. The (1 0 3), (1 1 0), and (Z3) planes had the second-highest TC values for sample Z3, whereas the (1 0 1) plane showed substantial preferential growth. The second-highest TC value for the (1 1 2) plane was also observed in Sample Z4, along with the (1 1 0) and (1 0 1) planes. Fig. 2 represents a schematic diagram of the crystallographic planes for the hexagonal unit cell of ZnO.

$$\text{Preference growth, } P = \frac{\text{RI}_{\text{sample}} - \text{RI}_{\text{standard}}}{\text{RI}_{\text{standard}}} \tag{7}$$
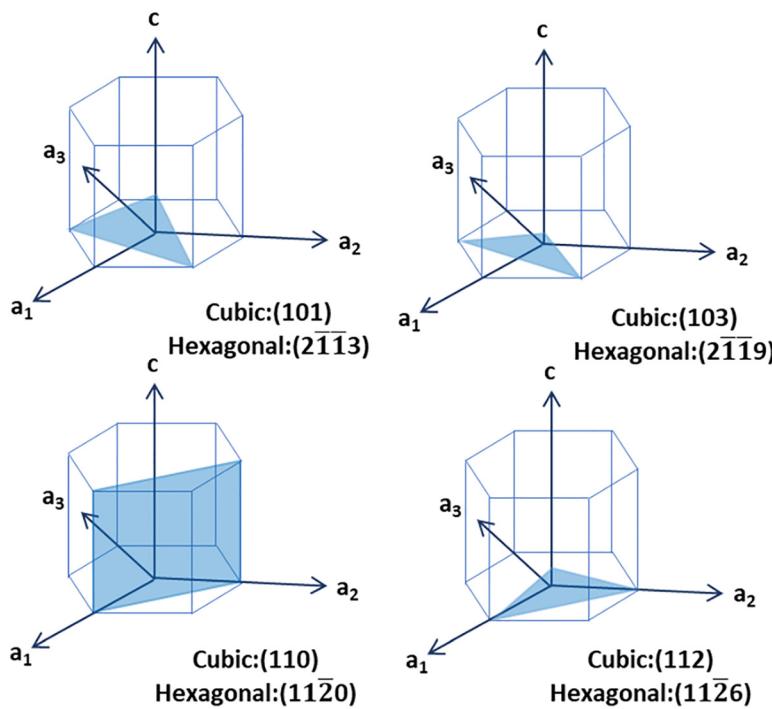

Fig. 1 The X-ray pattern of Z1, Z2, Z3, and Z4 ZnO-NPs.

Fig. 2 A visual representation of hexagonal ZnO's crystallographic planes (101), (103), (110), and (112).

$$\text{Texture coefficient, } TC = \frac{\frac{I}{I_0}}{\frac{1}{N}\sum_1^N \frac{I}{I_0}} \quad (8)$$

Here, RI refers to relative intensity, I_0 and I are denoted for average intensity and relative intensity for a particular plane, respectively, and N is denoted for the reflected numbers.

For the (101), (110), and (103) planes, positive preferred growth was consistently seen; Z1 and Z2 showed the highest values. The preference development was positive for the (112) plane for the Z2 and Z4 samples. The differences in texture coefficients highlight how atomic density deviations and XRD intensity are related to atomic structural parameters that affect intensity for particular planes. The texture coefficient change illustrates the relationship between the atomic density deviation of a given plane and XRD intensity, where the atomic structure factors are related to the XRD intensity.

For each sample, the phase analysis parameter values and the texture coefficient and preference growth for six distinct ZnO-NP planes are displayed in Tables 1 and 2. The estimated crystallite sizes are recorded in Table S1 (ESI†).

3.2 Field emission scanning electron microscopy (FESEM)

ZnO nanoparticles (ZnO-NPs) can be hexagonal, spherical, quasi-spherical, agglomerated rod-shaped, cubic, or irregular platelet-shaped, among other shapes.[21] High-resolution field emission scanning electron microscopy was used to create the FESEM image in Fig. 3, which demonstrates significant variations across all samples. The nanodisc in Z1 has a uniformly smooth surface. Consistent with earlier observations, the agglomerated ZnO nanocrystallites exhibit spherical, densely packed, randomly split particles with an average diameter ranging from 40 nm to 240 nm.[22–25] Z2 exhibits slightly cubic-shaped rod particles, indicating a 3D morphology. Z3 reveals a combination of plate-like and needle-like structures, consistent with previously reported ZnO morphologies.[26] A neatly arranged rod-shaped structure may be seen in Z4. Variations in the generated ZnO nanoparticles' sizes and shapes improve their

Table 1 Different crystallographic parameters for Z1, Z2, Z3, and Z4

Parameter	Z1	Z2	Z3	Z4
Crystallite size, D_c, nm	34.40	84.51	36.69	97.20
Dislocation density, (10^3 lines per m²)	0.85	0.14	0.75	0.11
Micro-strain, ε	0.1394	0.0816	0.1334	0.0611
Lattice parameter, Å	$a = 3.2546$	3.2529	3.2557	3.2510
	$c = 5.2064$	5.2103	5.21198	5.2068
Volume of unit cell, Å³	47.76	47.75	47.84	47.66
Specific surface area, S, m² g⁻¹	31.12	12.66	29.17	11.01
Relative intensity, RI	0.7565	0.7331	0.7283	0.7207
Preference growth, P	0.2634	0.2247	0.2163	0.2038

Table 2   Texture coefficient of the ZnO-NPs

Sample	Planes			Preference growth	Texture coefficient, TC	Observation
Z1	1	0	1	0.2633	1.22	101, 110, 103, and 112 texturing
	1	0	0	−0.0987	0.98	
	0	0	2	−0.2403	0.85	
	1	1	0	0.0441	1.10	
	1	0	3	0.0973	1.16	
	1	1	2	−0.0335	1.02	
Z2	1	0	1	0.2242	1.12	101, 110, 103, and 112 texturing
	1	0	0	−0.0870	0.93	
	0	0	2	−0.2232	0.81	
	1	1	0	0.0614	1.04	
	1	0	3	0.0398	1.02	
	1	1	2	0.1353	1.12	
Z3	1	0	1	0.2162	1.18	101, 110, 103, and 112 texturing
	1	0	0	−0.1052	0.97	
	0	0	2	−0.1453	0.93	
	1	1	0	−0.0070	1.04	
	1	0	3	0.07737	1.13	
	1	1	2	−0.0122	1.04	
Z4	1	0	1	0.2035	1.13	101, 110, and 112 texturing
	1	0	0	−0.0641	0.96	
	0	0	2	−0.19433	0.85	
	1	1	0	0.0158	1.02	
	1	0	3	−0.0290	0.98	
	1	1	2	0.0629	1.07	

surface area-to-volume ratio and, consequently, their antibacterial and photocatalytic effectiveness. ImageJ software was used to compute all metrics.

3.3   Elemental analysis by EDX

Through EDX spectrum analysis, which provided specifics on the chemical makeup of the green-synthesized ZnO-NPs, the purity of the ZnO nanoparticles (ZnO-NPs) was further verified. The purity of the produced ZnO-NPs was confirmed by this quantitative analysis, which only showed Zn and O peaks. The elemental composition of Zn and O in samples Z1, Z2, Z3, and Z4 revealed that the percentages of Zn and O atoms were 86.33%, 78.19%, 86.67%, and 87.07%, respectively, and 13.67%, 21.81%, 13.33%, and 12.93%, respectively. Three notable peaks between 1 and 10 kV were visible in the EDX spectra and validate the presence of both oxygen and zinc.

3.4   Detecting functional groups

A discernible absorption band can be found in the fingerprint region of the FTIR spectrum. The absorption bands beneath 1000 cm^{-1} are often where metal-oxide materials are found due to interatomic vibrations. The peaks at about 544, 545, and 558 cm^{-1} could be caused by observed metal–oxygen (M–O) stretching modes of vibration. In Fig. 4, noticeable bands about 550 cm^{-1} indicate the current Zn–O stretching mode.[27] The additional peaks at 1373, 1375, and 1060 cm^{-1} indicate the C=O and C–O vibration modes and could be the consequence of improper carbonate group breakdown.[28] The instrument's detection of ambient CO$_2$ falls within the band 2364 cm^{-1}.[29]

3.5   Raman spectroscopy

Numerous distinctive peaks of wurtzite-phase ZnO can be seen in the Raman spectra in Fig. S1 (ESI†) of the ZnO nanoparticle samples. The E2 (low) mode is responsible for the strong peak at about 97 cm^{-1}, whereas multi-phonon scattering is frequently associated with the intense peak at about 334 cm^{-1}.[30,31] The large peak shows the highly crystalline hexagonal structure at about 439 cm^{-1}, which corresponds to the E2 (high) mode.[32] Furthermore, the A1(LO) or E1(LO) band modes close to 588 cm^{-1} can be
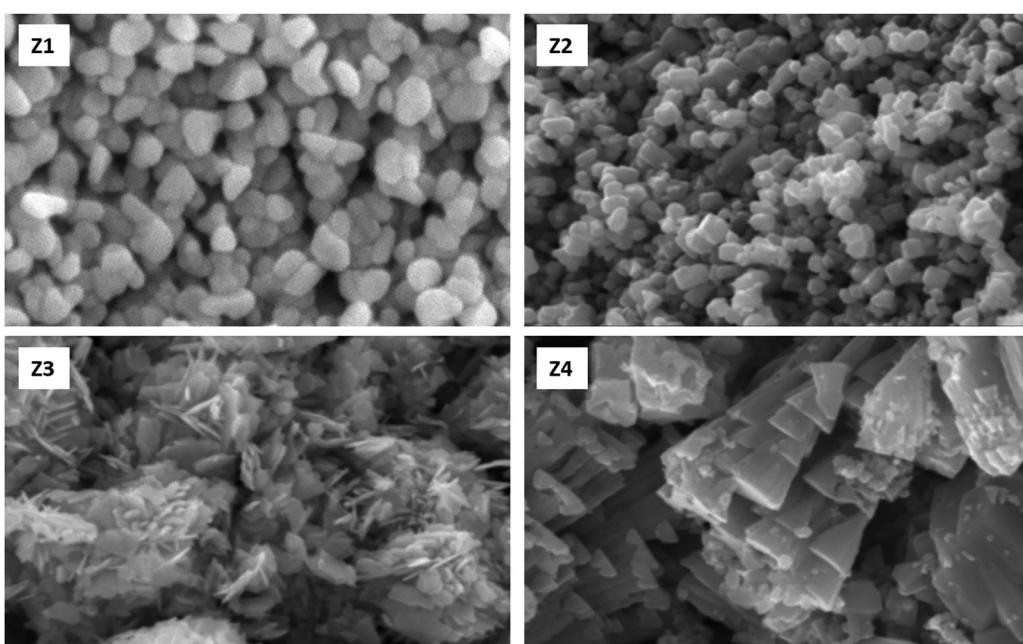

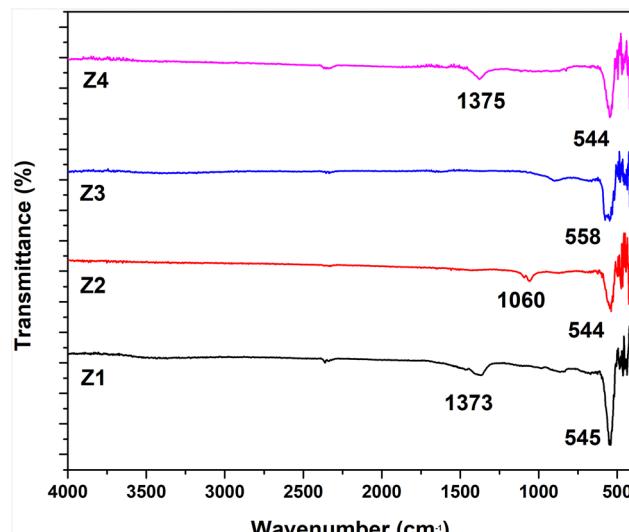**Fig. 3**   FESEM images of Z1, Z2, Z3 and Z4 ZnO-NPs.

Fig. 4 FTIR spectrum of the synthesized ZnO-NPs.

identified.[33] These spectral characteristics, which show few indications of contaminant phases, validate the ZnO nanoparticles' purity and phase identity.

3.6 Anti-microbial test

Both Gram-positive *Staphylococcus aureus* and Gram-negative *Escherichia coli* were susceptible to the antibacterial action of ZnO nanoparticles (Fig. 5). *S. aureus* displayed the biggest inhibitory zones among the investigated microorganisms, as demonstrated in Table 3. Interestingly, sample Z2 showed the strongest antibacterial activity against both microorganisms. On the other hand, samples Z1 and Z4 showed similar inhibitory zones for *E. coli* and *S. aureus*. Out of all the examined samples, Z3 showed the smallest zone of inhibition. This implies that depending on the production process, particle properties, or structural alterations, ZnO nanoparticles' antibacterial efficacy can vary greatly.

3.7 Photocatalytic activity analysis

ZnO can demonstrate photocatalytic activity when exposed to different light wavelengths (UV-visible light, infrared, *etc.*) that stimulate electron–hole pairs because of the conduction and valence bands in its electrical structure. For a duration of
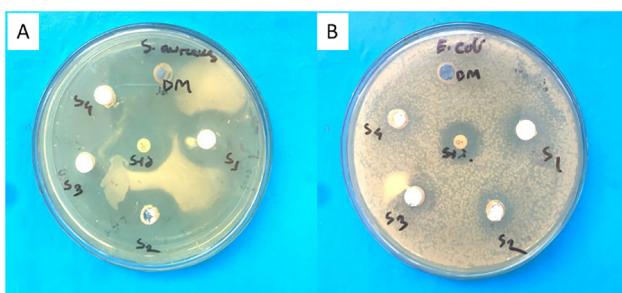

Fig. 5 Anti-microbial activity of ZnO NPs (S1 = Z1, S2 = Z2, S3 = Z3, and S4 = Z4) against (A) *S. aureus*, and (B) *E. coli*.

Table 3 Antibacterial activity of ZnO-NPs

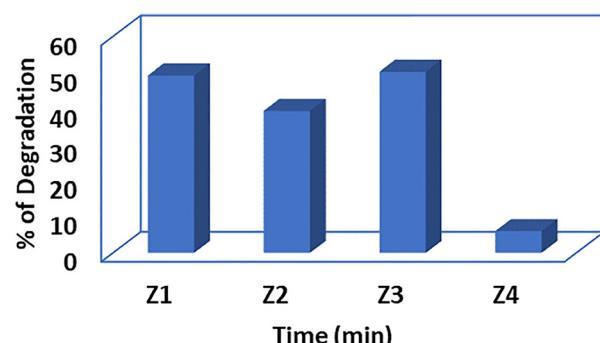| | Name of tested microorganisms | |
| | Gram-positive | Gram-negative |
| | Diameter of Zone of Inhibition (mm) | |
Sample name	*S. aureus*	*E. coli*
Z1	28	16
Z2	34	18
Z3	26	14
Z4	34	10
Positive control	26	20

Fig. 6 The dye removal percentage of ZnO-NPs in terms of time.

90 minutes, Fig. 6 displays the photocatalytic degradation efficiency of various ZnO samples (Z1, Z2, Z3, Z4) for Congo red dye (10 ppm). The maximum deterioration is seen in Z1 and Z3, which reach approximately 49% and 50%, respectively, suggesting higher photocatalytic activity. With a degradation of about 39%, Z2 has moderate activity, whereas Z4 has the lowest efficiency, with a degradation of less than 10%. Particle size, shape, or synthesis technique variations could be the cause of the performance variance. The most successful ZnO nanoparticles for removing Congo red dye were Z1 and Z3, demonstrating the promise of these particles for wastewater treatment applications.

Discussion

The relationship between the structural properties, functional performance, and production methods of zinc oxide nanoparticles (Z1–Z4) emphasizes the importance of morphological and crystallographic engineering in tailoring their applications. The nanoparticles were made using four distinct techniques: PEG-assisted co-precipitation (Z1), oleic acid-modified hydrothermal synthesis (Z2), conventional hydrothermal growth (Z3), and green synthesis using *Canna indica* extract (Z4). These techniques resulted in varying crystallite sizes, defect densities, and exposed crystal planes. XRD and FESEM investigations demonstrate that these structural changes have a direct effect on their antibacterial activity and photocatalytic dye degradation. For instance, Z1 and Z3 showed fragmented morphologies such as mixed plate-needle structures (Z3) and agglomerated

nanodiscs (Z1) because of their higher dislocation densities (0.85×10^3 and 0.75×10^3 lines per m^2), smaller crystallite sizes (34.4 nm and 36.7 nm, respectively), and higher microstrain (0.1394 and 0.1334). Their remarkable photocatalytic effectiveness, which led to 49% and 50% degradation of Congo red dye, respectively, was associated with these features.[34,35] On the other hand, Z2 and Z4 exhibited elongated morphologies, cubic rods for Z2, and well-defined nanorods for Z4, that were consistent with their increased antimicrobial activity, especially against *Staphylococcus aureus* (34 mm inhibition zones for both), despite having larger crystallites (84.5 nm and 97.2 nm), smoother surfaces, and lower defect densities (0.14×10^3 and 0.11×10^3 lines per m^2).[7]

The texture coefficient (TC) study revealed the preferential growth of particular crystallographic planes, which further clarified the structure-function link. High-energy, defect-rich facets with asymmetric atomic configurations, the (1 0 1) and (1 0 3) planes (TC = 1.16–1.13), were dominant in Z1 and Z3. Because these planes provide localized electric fields that improve charge carrier separation, they encourage photocatalytic activity.[36,37] For instance, photogenerated electrons and holes are trapped by oxygen vacancies and interstitial zinc atoms, which lowers recombination rates and extends the lifespan of reactive oxygen species (ROS) such as superoxide ions ($^{\bullet}O_2{}^-$) and hydroxyl radicals ($^{\bullet}OH$).[38,39] Through a multi-step process, these radicals propel the oxidative destruction of organic pollutants such as Congo red. The dye is mineralized into innocuous byproducts by visible light stimulation, which creates electron–hole pairs and redox processes in which holes oxidize water to $^{\bullet}OH$ and electrons decrease oxygen to $^{\bullet}O_2{}^-$.[40] This process is further enhanced by Z1 and Z3's nanodisc and plate-like geometries, which maximize surface area and light absorption while offering a large number of active sites for interfacial interactions.

In contrast, the (1 1 2) and (1 1 0) planes (TC = 1.12–1.04), which are distinguished by homogeneous atomic packing and lower surface energy, showed preferred exposure in Z2 and Z4.[41] The stepped edges and defect-rich surfaces of Z2's (112) plane allow for the prolonged release of zinc ions (Zn^{2+}), which is essential for antibacterial activity. By attaching to thiol groups in enzymes and producing ROS, which oxidize lipids, proteins, and DNA, Zn^{2+} ions break through bacterial membranes through electrostatic interactions and interfere with cellular functions.[42] Furthermore, bacterial cell walls are physically punctured by the elongated cubic-rod (Z2) and nanorod (Z4) morphologies, especially in Gram-positive *S. aureus*, whose thick peptidoglycan layer is susceptible to mechanical stress.[43] Z4's nanorods' high aspect ratio improves their adherence to bacterial membranes, extending contact time and ion release.[44] However, because larger crystallites with fewer flaws lower redox-active sites, Z4's limited dye degradation (10%) can be explained by the structural stability at the expense of photocatalytic efficacy.

These structural results were mostly determined by the synthesis techniques. As a steric stabilizer, PEG promoted the anisotropic growth of nanodiscs with exposed (1 0 3) planes and prevented agglomeration in Z1's production.[45] During hydrothermal synthesis, oleic acid in Z2 stabilized the high-energy

(1 1 2) plane and encouraged the production of cubic rods by selectively capping specific facets.[46] For Z3, hydrothermal conditions enabled regulated nucleation and high-pressure growth, leading to heterogeneous morphologies and strained lattices with (1 0 1) planes predominating.[47] Stable nanorods were produced by green synthesis employing *Canna indica* extract (Z4), which introduced biomolecular capping agents that passivated reactive facets, favoring low-energy (1 1 0) and (1 1 2) planes.[48] These tactics highlight how crucial synthesis parameters are in adjusting surface energy and crystallographic orientation. These parameters include capping agents, temperature, and reaction kinetics.

The performance of antibacterial and photocatalytic processes is traded off due to conflicting structural needs. High surface area and defect density, as in Z1 and Z3, limit sustained ion release for antibacterial application by compromising structural stability while increasing photocatalytic activity. The bigger crystallites and low defect concentrations of Z2 and Z4, on the other hand, promote mechanical membrane disruption and regulated Zn^{2+} release while lowering redox activity. This dichotomy emphasizes how application-specific design is essential. In wastewater treatment, for example, when quick pollutant breakdown is essential, Z1 and Z3 are perfect, but Z2 and Z4 are appropriate for biomedical applications that need long-term antibacterial activity.

These results are supported by a comparison with the literature. Research has connected the defect-rich (1 0 3) plane to improved charge separation in photocatalysis, which is in line with the functionality of Z1 and Z3. ZnO nanorods' antibacterial activity also supports studies that highlight the significance of shape in bacterial membrane penetration. But the (1 1 2) plane's dual role in Z2—mediating both surface reactivity and ion release—is a fresh discovery that raises the possibility of its use in multipurpose applications.

Conclusion

This work illustrates how important synthesis pathways are for customizing ZnO-NP's shape, functionality, and crystallography. The four separate synthesis techniques produced a freshly experienced plane with significantly varying crystallite sizes, defect concentrations, and favored crystallographic orientations (112). The (112) plane was identified as a novel contributor to both actions, establishing a connection between high surface reactivity and multifunctional performance, in addition to the other crystal planes' crucial roles in damage to bacterial membranes and enhancing photocatalytic dye degradation. The antibacterial efficacy of the (112) plane was attributed to its preferential exposure, which improved ion release and bacterial membrane contacts. Due to competing structural constraints, the study also emphasizes a trade-off between photocatalytic and antibacterial capabilities. Defect-rich structures may hamper stability for long-term antibacterial activity, even though they increase photocatalytic efficiency. Larger, more distinct morphologies, on the other hand, enhance antibacterial activity

while reducing photocatalytic reactivity. These findings imply that by choosing suitable synthesis techniques, ZnO-NPs can be customized for certain uses. Future studies could investigate hybrid nanostructures or doping techniques to improve multi-functionality and optimize ZnO-NPs for environmental and biological uses. This research advances the logical design of ZnO-based materials and facilitates their efficient application in practical situations.

Author contributions

Priya Paul synthesized and characterized the ZnO, executed the experiment, and wrote the draft and original manuscript. Md. Sahadat Hossain conceived and designed the experiment, analyzed the data and supervised the work. Newaz Mohammed Bahadur visualized the whole research. Muhammad Shahriar Bashar helped in the SEM analysis. Nazmul Islam Tanvir executed the Raman analysis. Subarna Sandhani Dey performed a formal analysis. Fataha Nur Robel and Samina Ahmed supervised the findings of this work. Samina Ahmed supervised the overall work and managed the required facilities.

Data availability

Data will be made available by the authors upon request.

Conflicts of interest

There are no conflicts to declare.

Acknowledgements

References

1 N. B. Singh, B. Kumar, U. L. Usman and Md. A. B. H. Susan, *Nano-Struct. Nano-Objects*, 2024, **39**, 101299.

2 F. Güell, A. Galdámez-Martínez, P. R. Martínez-Alanis, A. C. Catto, L. F. Da Silva, V. R. Mastelaro, G. Santana and A. Dutt, *Mater. Adv.*, 2023, **4**, 3685–3707.

3 L.-Y. Wang, B.-Y. Shi, C.-B. Yao, Z.-M. Wang, X. Wang, C.-H. Jiang, L.-F. Feng and Y.-L. Song, *ACS Appl. Nano Mater.*, 2023, **6**, 9975–10014.

4 S. R., S. N. Kumar, M. R. M., J. Pattar and D. R. B. V., *J. Mater. Chem. B*, 2024, **12**, 2180–2196.

5 V. Harish, M. M. Ansari, D. Tewari, A. B. Yadav, N. Sharma, S. Bawarig, M.-L. García-Betancourt, A. Karatutlu, M. Bechelany and A. Barhoum, *J. Taiwan Inst. Chem. Eng.*, 2023, **149**, 105010.

6 K. Bisaria, S. Sinha, R. Singh and H. M. N. Iqbal, *Chemosphere*, 2021, **284**, 131263.

7 F. Y. Rezaei, G. Pircheraghi and V. S. Nikbin, *ACS Appl. Nano Mater.*, 2024, **7**, 15242–15254.

8 H. Jubair and M. Mehenaz, 2025, preprint, DOI: **10.22541/au.173956833.32066019/v1** (Server name: **https://www.authorea.com/preprints**).

9 G. R. Khan, *Appl. Phys. A: Mater. Sci. Process.*, 2020, **126**, 311.

10 N. Wu, J. Wang, D. N. Tafen, H. Wang, J.-G. Zheng, J. P. Lewis, X. Liu, S. S. Leonard and A. Manivannan, *J. Am. Chem. Soc.*, 2010, **132**, 6679–6685.

11 G. Liu, H. G. Yang, J. Pan, Y. Q. Yang, G. Q. (Max) Lu and H.-M. Cheng, *Chem. Rev.*, 2014, **114**, 9559–9612.

12 G. Kaur, A. Mitra and K. L. Yadav, *Prog. Nat. Sci.: Mater. Int.*, 2015, **25**, 12–21.

13 M. S. Hamdy, K. V. Chandekar, M. Shkir, S. AlFaify, E. H. Ibrahim, Z. Ahmad, M. Kilany, B. M. Al-Shehri and K. S. Al-Namshah, *J. Nanostruct. Chem.*, 2021, **11**, 147–163.

14 K. Chen, J. Li, W. Wang, Y. Zhang, X. Wang and H. Su, *Mater. Sci. Semicond. Process.*, 2012, **15**, 20–26.

15 P. Chandrasekaran, G. Viruthagiri and N. Srinivasan, *J. Alloys Compd.*, 2012, **540**, 89–93.

16 M. Pirsaheb, T. Gholami, H. Seifi, E. A. Dawi, E. A. Said, A.-H. M. Hamoody, U. S. Altimari and M. Salavati-Niasari, *Environ. Sci. Pollut. Res.*, 2024, **31**, 24768–24787.

17 A. Ejsmont and J. Goscianska, *Materials*, 2023, **16**, 1641.

18 B. M. Nizar, M. Lajnef, J. Chaste, R. Chtourou and E. Herth, *RSC Adv.*, 2023, **13**, 15077–15085.

19 Z. A. Ali, I. Shudirman, R. Yahya, G. Venkatraman, A. H. Hirad and S. A. Ansari, *Crystals*, 2022, **12**, 1808.

20 Md Sahadat Hossain and S. Ahmed, *Results Mater.*, 2023, **20**, 100492.

21 A. W. Alshameri and M. Owais, *OpenNano*, 2022, **8**, 100077.

22 R. S. Sabry, W. J. Aziz and M. I. Rahmah, *J. Inorg. Organomet. Polym.*, 2020, **30**, 4533–4543.

23 S. Thambidurai, P. Gowthaman, M. Venkatachalam, S. Suresh and M. Kandasamy, *J. Alloys Compd.*, 2021, **852**, 156997.

24 Z. Aalami, M. Hoseinzadeh, P. Hosseini Manesh, A. H. Aalami, Z. Es'haghi, M. Darroudi, A. Sahebkar and H. A. Hosseini, *Heliyon*, 2024, **10**, e24212.

25 M. S, H. N and V. PP, *BioNanoSci.*, 2020, **10**, 112–121.

26 Y. Sheng, Y. Jiang, X. Lan, C. Wang, S. Li, X. Liu and H. Zhong, *J. Nanomater.*, 2011, **2011**, 1–12.

27 T. Ahmad, V. Pandey, M. Saddam Husain, Adiba and S. Munjal, *Mater. Today: Proc.*, 2022, **49**, 1694–1697.

28 P. T. Thu, V. D. Thinh, V. D. Lam, T. N. Bach, L. T. H. Phong, D. H. Tung, D. H. Manh, N. Van Khien, T. X. Anh and N. T. H. Le, *Catalysts*, 2022, **12**, 801.

29 I. Elhamdi, H. Souissi, O. Taktak, J. Elghoul, S. Kammoun, E. Dhahri and B. F. O. Costa, *RSC Adv.*, 2022, **12**, 13074–13086.

30 A. Momot, M. N. Amini, G. Reekmans, D. Lamoen, B. Partoens, D. R. Slocombe, K. Elen, P. Adriaensens, A. Hardy and M. K. Van Bael, *Phys. Chem. Chem. Phys.*, 2017, **19**, 27866–27877.

31 B. N. Mavrin, L. N. Demyanets and R. M. Zakalukin, *Phys. Lett. A*, 2010, **374**, 4054–4056.

32 I. Calizo, K. A. Alim, V. A. Fonoberov, S. Krishnakumar, M. Shamsa, A. A. Balandin and R. Kurtz, in *Micro-Raman spectroscopic characterization of ZnO quantum dots, nanocrystals, and nanowires*, ed. K. G. Eyink, D. L. Huffaker and F. Szmulowicz, San Jose, CA, 2007, 64810N.

33 A. K. Ojha, M. Srivastava, S. Kumar, R. Hassanein, J. Singh, M. K. Singh and A. Materny, *Vib. Spectrosc.*, 2014, **72**, 90–96.

34 L. Nadjia and E. Abdelkader, *J. Iran. Chem. Soc.*, 2025, **22**, 297–324.

35 S. Sivakumar, Y. Robinson and N. A. Mala, *Appl. Surf. Sci. Adv.*, 2022, **12**, 100344.

36 T. Zhou, M. Hu, J. He, R. Xie, C. An, C. Li and J. Luo, *CrystEngComm*, 2019, **21**, 5526–5532.

37 R. Y. Hong, J. H. Li, L. L. Chen, D. Q. Liu, H. Z. Li, Y. Zheng and J. Ding, *Powder Technol.*, 2009, **189**, 426–432.

38 K. R. Raghupathi, R. T. Koodali and A. C. Manna, *Langmuir*, 2011, **27**, 4020–4028.

39 K. S. Siddiqi, A. Ur Rahman, Tajuddin and A. Husen, *Nanoscale Res. Lett.*, 2018, **13**, 141.

40 A. Chakravorty and S. Roy, *Sustain. Chem. Environ.*, 2024, **8**, 100155.

41 H. Funakubo, N. Mizutani, M. Yonetsu, A. Saiki and K. Shinozaki, *J. Electroceram.*, 1999, **4**, 25–32.

42 C. A. Juan, J. M. Pérez De La Lastra, F. J. Plou and E. Pérez-Lebeña, *Int. J. Mol. Sci.*, 2021, **22**, 4642.

43 J. Ye, B. Li, Y. Zheng, S. Wu, D. Chen and Y. Han, *Bioact. Mater.*, 2022, **15**, 173–184.

44 S. G. Higgins, M. Becce, A. Belessiotis-Richards, H. Seong, J. E. Sero and M. M. Stevens, *Adv. Mater.*, 2020, **32**, 1903862.

45 P. R. Sajanlal, T. S. Sreeprasad, A. K. Samal and T. Pradeep, *Nano Rev.*, 2011, **2**, 5883.

46 L. T. Su, J. Ye, S. K. Karuturi, L. Liu, Y. Zhao, J. Guo, L. F. N. Ah Qune, T. C. Sum and A. I. Y. Tok, *CrystEngComm*, 2011, **13**, 5367.

47 M. Shandilya, R. Rai and J. Singh, *Adv. Appl. Ceram.*, 2016, **115**, 354–376.

48 A. A. Akinsiku, E. O. Dare, O. O. Ajani, J. Ayo-Ajayi, O. T. Ademosun and S. O. Ajayi, *IOP Conf. Ser.: Earth Environ. Sci.*, 2018, **173**, 012019.